Local structure effects of carbon-doping on the phase change material $Ge_2Sb_2Te_5$

Journal:	*Journal of Materials Chemistry C*
Manuscript ID	TC-ART-03-2024-001082.R1
Article Type:	Paper
Date Submitted by the Author:	26-Apr-2024
Complete List of Authors:	Langhout, John; University of Florida, Materials Science and Engineering Alverson, Danielle; University of Florida, Materials Science and Engineering Ginter, Colton; University of Florida, Materials Science and Engineering Ravel, Bruce; National Institute of Standards and Technology Adams, David; Sandia National Laboratories, Materials Science and Engineering Center Butala, Megan; University of Florida, Materials Science and Engineering

Local structure effects of carbon-doping on the phase change material $Ge_2Sb_2Te_5$

John D. Langhout,† Danielle N. Alverson,† Colton Ginter,† Bruce Ravel,‡ David Adams,¶ and Megan M. Butala*,†

†*Department of Materials Science and Engineering, University of Florida, Gainesville, FL 32611*

‡*Material Measurement Laboratory, National Institute of Standards and Technology, Gaithersburg, MD 20899, USA, ORCID: 0000-0002-4126-872X*

¶*Sandia National Laboratories, Albuquerque, New Mexico 87185 USA*

E-mail: mbutala@ufl.edu

Abstract

$Ge_2Sb_2Te_5$ is used in phase change memory, a nonvolatile memory technology, due to its phase change properties. The primary advantage of phase change memory over the state-of-the-art (flash memory) is its simple and small device geometry, which allows for denser nodes and lower power consumption. In phase change memory, resistive heating induces fast switching between the high resistance amorphous and low resistance crystalline phases, corresponding to storage of low and high digital states, respectively. However, the instability of the amorphous phase of $Ge_2Sb_2Te_5$ presents issues with processing and long-term data storage; such issues can be resolved by C doping, which stabilizes the amorphous phase and raises the crystallization temperature. To better understand the local structural effects of C doping on $Ge_2Sb_2Te_5$, *in situ* Ge *K*-edge X-ray absorption spectroscopy measurements were taken during heating of films with various C doping concentrations. The range of structural transformation temperatures derived from X-ray absorption near-edge structure analysis across the C doping series proved narrower than crystallization temperatures reported in similar *in situ* X-ray diffraction experiments, which may reflect changes in local structure that precede long-range ordering during crystallization. In addition, rigorous extended X-ray absorption fine structure fitting across and between temperature series revealed effects of C doping on the rigidity of Ge−Te bonds at low (2 at% and 4 at%) C concentrations.

Introduction

Phase change memory has been identified as a promising alternative to existing non-volatile memory technologies.[1–7] Phase change memory cells are composed of a volume of phase change material that switches between crystalline (conductive) and amorphous (resistive) phases. These phases are used to store high and low digital states, respectively, and the phase changes are driven through resistive heating pulses.[1,5,8–10] The implementation of phase change memory cells is more simple and scalable than existing flash memory cells (e.g., floating gate cells), allowing for higher device density, lower power consumption, and lower device cost.[2,5–7,9,11–13]

The leading candidate material for optimization of phase change memory is $Ge_2Sb_2Te_5$ (GST), a chalcogenide with fast crystallization and amorphization rates, as well as high resistivity contrast between its crystalline and amorphous states.[1,3–8,14–16] A shortcoming of GST for use in phase change memory is the poor phase stability of its amorphous state. Specifically, the relatively low crystallization temperature of GST ($\approx 140\,^{\circ}\mathrm{C}$) can result in unwanted crystallization during processing, high-temperature use, or long-term use.[6,10,13,15,17] Accordingly, increasing the crystallization temperature of GST is essential for its optimization for phase change memory.

One effective approach for increasing the crystallization temperature of chalcogenide phase change materials is through the incorporation of dopants, typically nitrogen,[10,18–21] oxygen,[22] and carbon.[2,13–17,23–25] However, how these dopants modify structure and properties is not well understood. For GST, carbon is a well-studied dopant, but there is not yet a consensus of how carbon is incorporated in the amorphous or crystalline structures, nor of the mechanism by which carbon modifies phase change behavior, especially crystallization temperature.[15,16] Improved understanding of the interdependencies between structure, composition, and properties would not only allow for the optimization of GST for phase change memory applications, but would also have broader implications for designing structure and function in other chalcogenide materials.

It is challenging to study the structure of amorphous materials or characterize light elements using X-rays independently; both are required in combination to understand the role of carbon in GST. X-ray absorption spectroscopy (XAS) provides access to local structure in the absence of long-range order, however, weakly scattering light elements (i.e., C, N, O) in low concentrations are challenging to probe when their scattering paths overlap with those containing heavier elements such as Ge, Sb, and Te. This issue presents a unique challenge for identifying how carbon modifies the behavior of GST, and more broadly, how light dopants are incorporated in amorphous materials. Indeed, GST is but one material among an abundance of amorphous chalcogenides with promise for memory applications, such as phase change memory[1,2,5–7,10,13–16,18,19,23] and ovonic threshold switching,[26–30] for which further structural understanding would benefit their development.

Here, we probe local structure changes during crystallization for GST and carbon-doped GST (GST-C) thin films at several compositions [$(Ge_2Sb_2Te_5)_{1-x}C_x$, where $x = 0.02$, 0.04, 0.06, and 0.12] using *in situ* Ge K-edge X-ray absorption spectroscopy. We see abrupt changes in the local environment of Ge upon crystallization, and a narrow range of structural transformation temperatures over the composition series relative to X-ray diffraction studies.[14] We posit that this difference reflects the different sensitivities of diffraction and spectroscopy to long-range and local atomic structure. From our analysis of *in situ* extended X-ray absorption fine structure (EXAFS) data, we also find the local environment of Ge changes before crystallization, and that the nature of these changes varies with carbon content. More specifically, we attribute this behavior to a modulation of the Ge−Te bond rigidity with the addition of carbon.

In addition to identifying structural insights specific to GST/GST-C, we develop a rigorous methodology with which to understand its temperature-dependent behavior while avoiding overfitting and other nonphysical fitting results. Of particular note, our methodology recognizes the physical limitations of EXAFS and accounts for parameter correlations by applying parameter fitting constraints and analysis of parameter trends, rather than focusing on parameter values directly. We anticipate that the materials insights and methodological practices we report here will benefit fundamental understanding and technological development for GST and related materials.

Results and Discussion

Ge K-edge X-ray absorption spectroscopy (XAS) data were collected on $\approx 300\,\mathrm{nm}$ thick as-deposited films of GST and carbon-doped (GST-C) during *in situ* heating. Carbon-doped films were prepared with compositions $(\mathrm{Ge_2Sb_2Te_5})_{1-x}\mathrm{C}_x$ with $x = 0.02$, 0.04, 0.06, and 0.12, referred to as GST-2%, GST-4%, GST-6%, and GST-12%, respectively. Amorphous films on fused silica substrates were heated from 30 °C to 300 °C, through crystallization to the cubic structure, with XAS data recorded at 10 °C increments, except for GST-12%, for which data were recorded from 110 °C to 300 °C.

X-ray Absorption Near Edge Structure

During heating, there is an abrupt change in the X-ray absorption near edge structure (XANES) for most compositions, with consistent edge and post-edge features representing the amorphous and crystalline phases (Fig. 1). This reflects the abrupt change in the Ge local environment, as is expected during phase change.[4] For 0% (GST), linear combination analysis shows that the transition of the edge occurs between 120 °C and 150 °C. This is indicated by a mixture of crystalline and amorphous spectrum features at 130 °C and 140 °C. In 2% and 4% doped samples, transitions of the spectra are more abrupt, occurring between 140 °C and 150 °C (Fig. S1). GST-6% behaves similarly to GST-0%, in which the spectrum at 150 °C has features from both amorphous and crystalline spectra, indicating a mixture of these two local environments. For GST-12%, XANES data do not qualitatively change through the measured temperature range, up to 300 °C (Fig. S2). In the context of previous work using X-ray diffraction (XRD), this is expected for GST-12%, reflecting that sufficiently high doping concentrations elevate the crystallization temperature, but also disrupt the fast switching mechanism of GST.[14]

XANES data for GST, GST-2%, GST-4%, and GST-6% were fit as linear combinations of their amorphous (lowest temperature) and crystalline (lowest temperature post-transformation) spectra (GST and GST-6% in Fig. 1, GST-2% and GST-4% in Fig. S1). Fitting results reflect the step-wise transformation of the spectra, emphasizing the abrupt transformation of GST-2%, and GST-4% between 140 °C and 150 °C, and the relatively gradual transformation of GST spectra between 120 °C and 150 °C and GST-6% between 140 °C and 160 °C.

The change in transformation temperature from *in situ* XANES data does not align with crystallization temperature (T_C) as derived from *in situ* XRD and resistivity measurements at similar C-doping concentrations. Previous work on similarly prepared films indicates an increase in T_C from 125 °C (GST) to 145 °C (GST-6%) based on *in situ* XRD analysis.[14] Literature consistently reports a T_C of ≈140 °C for GST,[15,17,31] based on observation of resistivity changes and/or the emergence of diffraction peaks during *in situ* heating. T_C measured for carbon-doped GST is typically between 180 °C[16,24,31] and 220 °C,[15] but values as high as 300 °C have been reported,[25] depending on carbon content, film preparation,[20] and film thickness.[31]

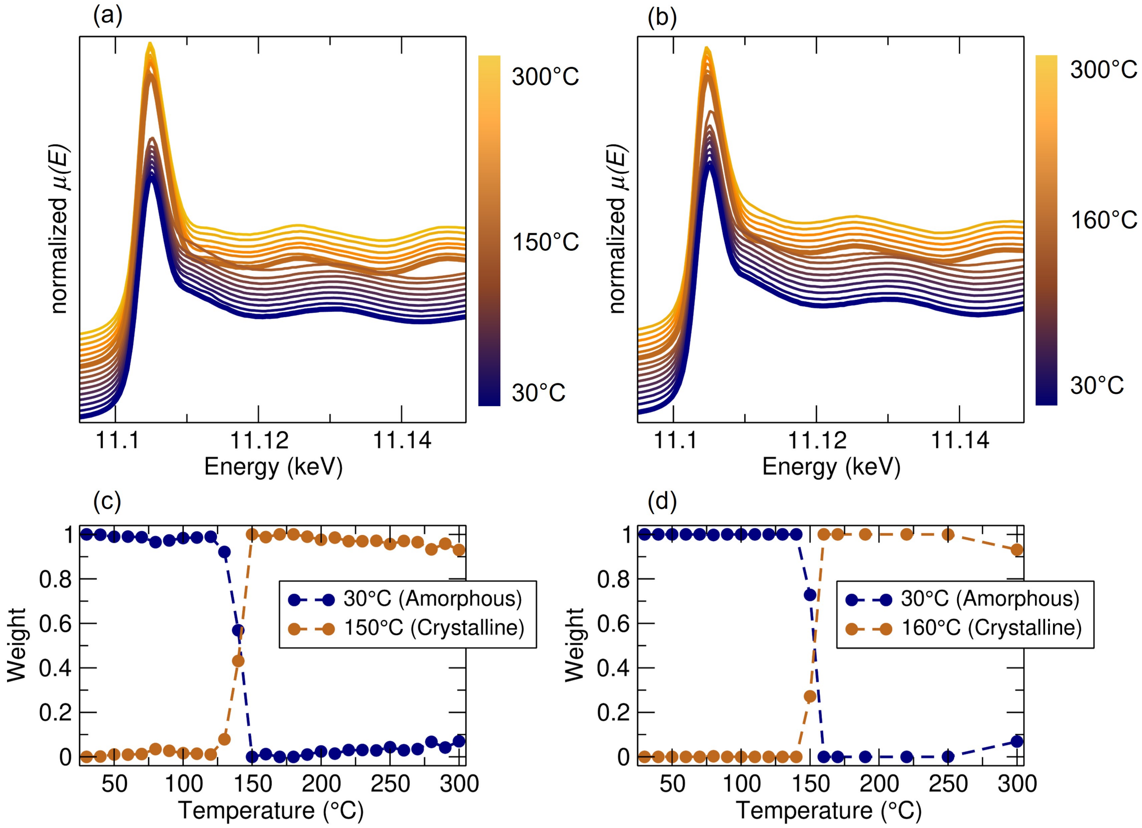

Figure 1: *In situ* XANES spectra for (a) GST and (b) GST-6% show changes in the white line intensity and post-edge features during heating. Representative 'amorphous' and 'crystalline' spectra for each composition were used as models for linear combination fitting of (c) GST and (d) GST-6% spectra, demonstrating the crystallization behavior. The percentage misfit is below 0.01% (1×10^{-4}) for all shown fits.

The disparity between the transformation temperatures detected using XAS and T_C as measured using XRD is most likely a result of the sensitivity to local and long-range structure of XAS and XRD, respectively. Using XRD, the crystallization temperature is defined as the temperature at which diffraction peaks emerge. Meanwhile, XAS is sensitive to the proportion of Ge atoms in local environments resembling the amorphous and crystalline phases. Macroscropic crystallinity is therefore not necessary for a material to 'look' crystalline in XAS data, for example, in the case of small crystallization seeds which precede the formation of crystallites.[32] In such a case, the material is beginning to crystallize, but is not yet crystalline. Thus, for the sake of accuracy, we will define the first temperature at which the XANES spectra begin to take on crystalline features as the 'crystallization onset temperature.'

Extended X-ray Absorption Fine Structure

In addition to the XANES region, XAS data were collected beyond the edge to enable Ge K-edge extended X-ray absorption fine structure (EXAFS) analysis, which provides additional information about the local Ge environment with respect to temperature and composition. In EXAFS, an X-ray at or above the edge energy of a given atom can cause that atom to emit a photoelectron. The interference between the outwardly propagating photoelectron and its scattering from surrounding atoms modulates the density of states, and thus the material's absorption coefficient.[10,33–35] Information about the photoelectron scattering paths, and accordingly the surrounding atoms, is contained in the EXAFS equation (Eq. 1), which gives the signal χ as a function of photoelectron momentum, k.

$$\chi\left(k\right) = S_0^2 \sum_i N_i \frac{f_i(k)}{kD_i^2} e^{\frac{2D_i}{\lambda(k)}} e^{-2k^2\sigma_i^2} \sin(2kD_i + \delta_i(k)) \tag{1}$$

Before crystallization, Fourier transformed EXAFS spectra for all GST/GST-C compositions have one intense feature centered at 2.5 Å, which corresponds to the first atomic coordination shell, and few discernible features beyond 3 Å (Fig. 2). These spectra are consistent with an amorphous material, in which single scattering paths of nearest-neighbor atoms dominate $|\chi(R)|$. At and above the crystallization onset temperature, spectra take a considerably different shape; the intensity of the first coordination feature decreases and the position shifts to a longer distance. Additionally, scattering paths beyond the first coordination shell emerge, indicating a higher degree of crystallinity (Fig. S5).

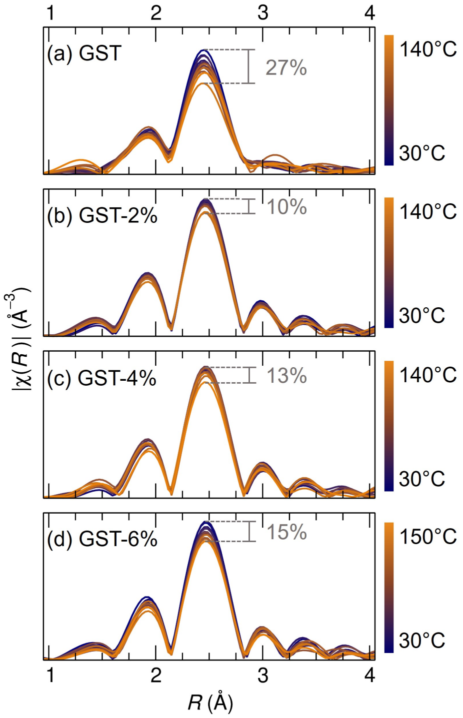

Figure 2: Temperature-dependent EXAFS spectra of amorphous (a) GST, (b) GST-2%, (c) GST-4%, and (d) GST-6% preceding crystallization show a decrease in the magnitude of $|\chi(R)|$ with increasing temperature. The percent reduction of the $|\chi(R)|$ maxima are labeled for each composition.

In addition to the pronounced changes in the Fourier transformed EXAFS spectra upon crystallization, there are also relatively subtle temperature-dependent changes in the spectra prior to crystallization. Specifically, in $|\chi(R)|$, the amplitude of the first-shell scattering path gradually dampens with increasing temperature for all compositions, indicating a change in the Ge local environment within the amorphous state. A decrease in the magnitude of $|\chi(R)|$ is expected with increasing temperature as a result of thermal vibrations, which broaden features and decrease their amplitude.[29,33,35–37] Notably, the extent of this dampening is composition-dependent; by measuring the change in the maximum $|\chi(R)|$ of the feature centered at 2.5 Å, we find a decrease in magnitude of 27% for GST and decreases of 10%, 13%, and 15% for GST-2%, GST-4%, and GST-6%, respectively (Fig. 2).

To better understand and quantify the temperature- and composition-dependent structural changes in amorphous GST and GST-C before crystallization, we fit EXAFS spectra using a least-squares method. In doing so, we considered several structural models, favoring those which balanced a low R-factor (the fitting figure of merit) with a reasonably low number of fitting parameters. The most successful models consisted of two single-scattering paths: a first-shell single scattering Ge−Te path and a first-shell single scattering Ge−Ge path.

The contribution of the first-shell single scattering Ge−C path was qualitatively visible near 1.4 Å in the amorphous EXAFS spectra of doped samples (Fig. S4). However, modeling this small feature is difficult since it is associated with a dilute and weakly scattering species. Further, modeling such short paths is inadvisable, since data in this region are strongly affected by background removal and can therefore be heavily distorted by the data reduction process.[10] For these reasons, we did not include a Ge−C path in fitting models.

EXAFS models consist of several fitting parameters, including the parameter ΔE_0, a correction term to the defined edge energy E_0, and the amplitude reduction factor ${S_0}^2$, which bears little meaning in our discussion as it is empirically derived and not directly related to atomic structure.[10,33,34] The value we used for ${S_0}^2$ (0.75) was determined from the best-fit model to GST and set constant when fitting other spectra. Three path-specific parameters are also added from each path in a model (e.g., the Ge−Te or Ge−Ge single scattering paths): N, the path degeneracy; r, the half path length; and σ^2, the mean square relative displacement parameter (akin to the Debye-Waller factor in diffraction analysis).[33,38] The models we used to fit amorphous EXAFS data comprise only single-scattering first-shell paths, such that the degeneracy, N, of each path is essentially the coordination of, in this case, Ge by either Ge or Te. Likewise, the half path length, r, for these first coordination single scattering paths is equivalent to the bond length for Ge−Te or Ge−Ge bonds, and σ^2 to the bond length variance.

To determine the origins of differences in EXAFS data as a function of composition and temperature for amorphous GST, we applied several approaches to fitting, which are described following. We first allowed path parameters to vary in unconstrained fitting, which we found to be unstable when applied over the temperature series. Instead, we constrained path parameters to minimize large swings of correlated parameters' values, from which we evaluated trends within and between each composition.

Unconstrained EXAFS Fitting

Room temperature Fourier transformed EXAFS spectra were fit using the Ge−Ge and Ge−Te paths with unconstrained parameters for each path (coordination values, bond lengths, and σ^2). The fits captured the features of the data well and the resulting values for N_{Ge-Te}, N_{Ge-Ge}, r_{Ge-Te}, and r_{Ge-Ge} were consistent with previous reports of the Ge environment in amorphous GST and GST-C at room temperature.[3,4,15] Representative room temperature $|\chi(R)|$ fits for GST and GST-2% are shown in Fig. 3 (fits for GST-4% and GST-6% can be found in Fig. S7) and refined parameter values for all low temperature fits are provided in Table S1.

To assess the extent of the changes in the local Ge environment with temperature, we applied the model fit to room temperature data to the rest of the amorphous data, tracking the relative goodness of fit, represented by the 'R-factor.' A smaller R-factor indicates a better fit, with an R-factor <0.02 generally corresponding to an acceptable fit of the model to the data.[33]

We used path parameters from unconstrained fits to each lowest temperature spectrum (30 °C for GST, GST-2%, and GST-6%; 40 °C for GST-4%) to generate representative models for each composition. These models were then 'fit' to spectra over the rest of the temperature

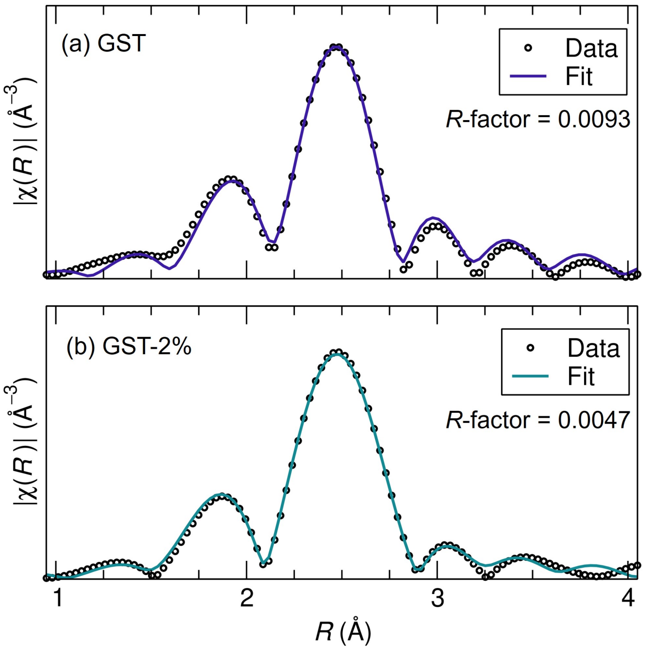

Figure 3: Low temperature (30°C) $|\chi(R)|$ spectra for amorphous (a) GST and (b) GST-2% fit between 1.5 Å and 3.5 Å to models using single-scattering paths for Ge−Ge and Ge−Te with all path parameters unconstrained. Visualization of per-path contributions are provided in Fig. S6.

series with all parameters fixed, except for ΔE_0. In this 'fixed fitting' approach, in which no parameters are refined, the increase of the R-factor with increasing temperature reflects the deviation of spectra from the room temperature model (Fig. 4).

When the resulting R-factors from these 'fits' are plotted as a function of temperature for each composition, temperature- and composition-dependencies become evident (Fig. 4). For room-temperature data, the fits have R-factors < 0.02, indicating excellent agreement between the data and the model (Fig. 3). With increasing temperature, the R-factor increases, reflecting a departure of the spectra from their low-temperature models, suggesting that the Ge environment changes significantly with temperature. Furthermore, this behavior is more severe in GST and GST-6%, which show steeper increases in R-factor, than in GST-2% and GST-4%, indicating a composition-dependence of the extent of the local change that precedes crystallization onset.

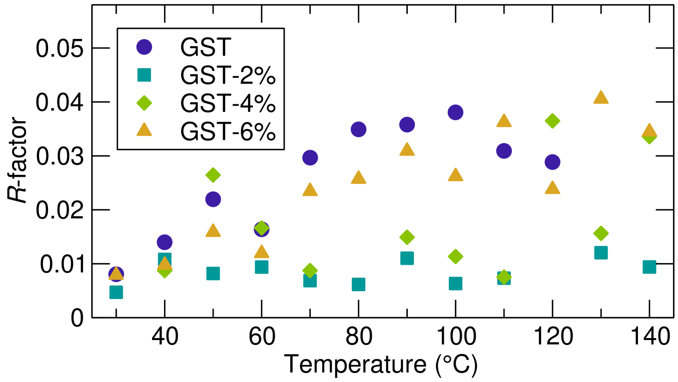

Figure 4: R-factor as a function of temperature for amorphous GST, GST-2%, GST-4%, and GST-6% using the 'fixed fitting' approach. The increase in R-factor reflects the change in the spectra with increasing temperature; this effect is greatest for GST and GST-6%. Some points are omitted due to inconsistencies in data quality. These omissions are discussed in greater detail in section 1.2 of the Supplementary Information.

Fitting the Temperature Series with Constrained Models

Applying a fixed model over the temperature series confirmed what was visualized in the *in situ* EXAFS data: the local Ge environment in the amorphous state changes *before* crystallization, and the extent of the change is composition-dependent. However, to understand the nature of these changes required a more robust approach.

Visually, the increase in R-factor in Fig. 4 can be attributed to the amplitude of $|\chi(R)|$ decreasing with increasing temperature, as seen in Fig. 2. This behavior is commonly observed in amorphous and crystalline materials alike; increasing dynamic atomic disorder due to temperature increases the variance of atomic correlation lengths, dampening the $\chi(R)$ signal. More specifically, this behavior is usually best captured using an Einstein model,[35–40] which assumes that the change in σ^2 is primarily due to the activation of optical phonon modes,[35] resulting in a nearly linear increase in σ^2 at temperatures above room temperature and across modest temperature ranges.

Testing whether GST and GST-C follow this well-studied behavior proved uniquely challenging. Since GST is amorphous, N_{Ge} and N_{Te} cannot be constrained to known coordination values from a crystal structure, so they must instead be refined as variables. Since both N and σ^2 contribute significantly to the magnitude of $\chi(R)$ of each path, the two parameters are highly correlated, leading to uncertainty in both terms.[33] Moreover, since the Ge−Te path and the Ge−Ge path are nearly the same length, their interference with each other causes the fit to be sensitive to their respective ratios.[10,35] Finally, N generally contains a high amount of uncertainty due to its correlation to ${S_0}^2$, the amplitude reduction factor. Without multiple shells to fit, ${S_0}^2$ was fixed to a constant value, and its uncertainty is transferred to N, with which it is statistically indistinguishable, following Eq. 1.[34] These three factors cause N and σ^2 to be highly correlated within and between paths. Fitting the temperature series with all four correlated parameters free to refine causes a high level of uncertainty, and sporadic, nonphysical parameter trends, highlighting the need for an alternate fitting approach.

To account for the change in EXAFS amplitude over each temperature series while avoiding strong parameter correlations and statistical uncertainty, we applied a constrained fitting approach. We fixed σ^2 for both paths over each temperature series, while the remaining parameters (ΔE_0, N, and r) were refined with no effective constraints. For each temperature series, the value of σ^2 for both paths was fixed to the value of the lowest temperature fit. By constraining σ^2, intensity changes of $|\chi(R)|$ were captured by changes in the values of N for each path.

This constrained fitting approach resulted in more stable, continuous trends in fitting parameters (N_{Ge} and N_{Te}) over the temperature series as a result of the reduced parameter correlations (Fig. 5). These fits also do not have the temperature-dependent increase in R-factor that resulted from applying a fixed model over the temperature range, indicating that the resulting models accounted for the temperature-dependent behavior of the EXAFS spectra. Further, the R-factor for fits for all compositions were reduced to near or below 0.02, indicating excellent agreement between the models and the data at all temperatures.

Plots of the product $N_{Ge-Te} \cdot \sigma^2_{Ge-Te}$ against temperature prior to crystallization show linear, negative relationships for each composition (Fig. 5a). Note that we report the constrained fitting data as a single value (the product of N and σ^2) since these highly correlated

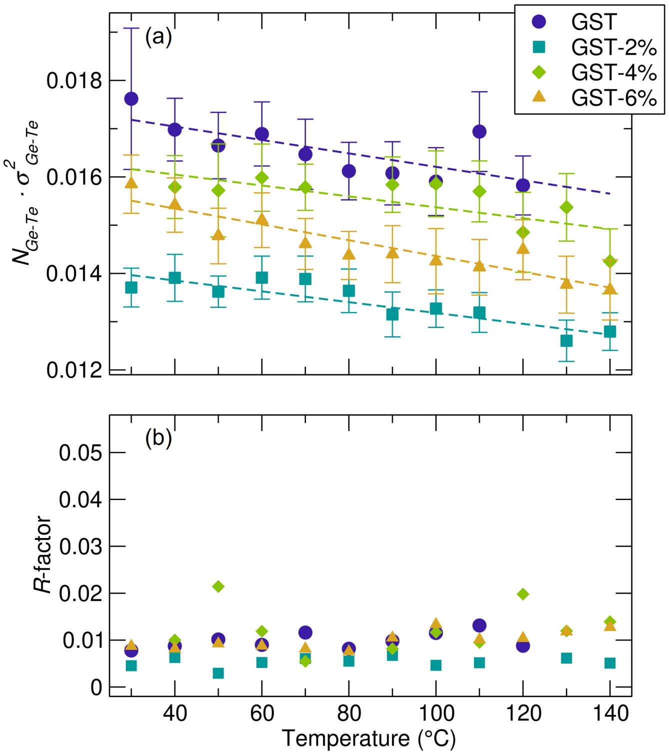

Figure 5: EXAFS fitting results for the constrained fitting method. (a) $N_{Ge-Te} \cdot \sigma^2_{Ge-Te}$ as a function of temperature for each composition show a linear decrease for all compositions, and steeper slopes for GST and GST-6%. Error bars denote standard error. (b) Resulting R-factors for constrained fits indicate excellent fits relative to fixed fitting (Fig. 4). Some fit values are omitted due to inconsistencies of data quality (see section 1.2 of Supplementary Information).

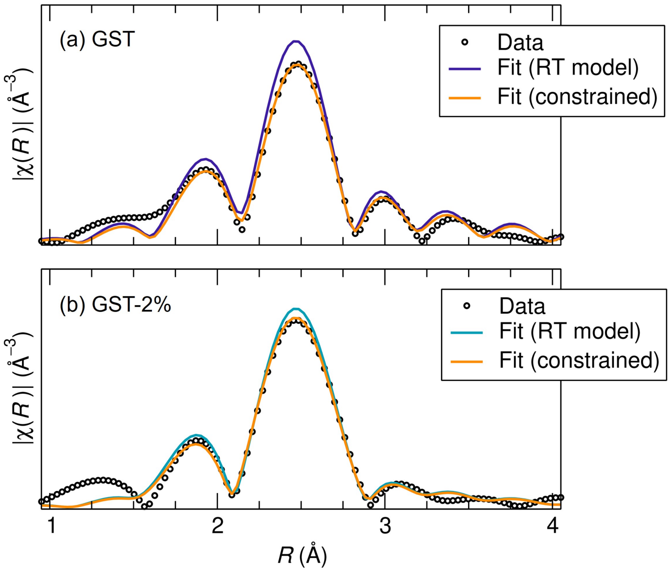

Figure 6: High temperature $|\chi(R)|$ spectra for amorphous (a) GST (120 °C) and (b) GST-2% (140 °C) fit between 1.5 Å and 3.5 Å using the 'fixed fitting' and constrained fitting approaches.

parameters must be considered in context of each other, and the precise values of N and σ^2 are ultimately arbitrary. Since N is negatively correlated with σ^2, this linear behavior can be explained by an increase in σ^2 and no change in N. Indeed, this behavior would coincide well with the aforementioned Einstein model for the relationship between σ^2 and temperature.[36–38,40] The alternative to this would be an increase in N and little-to-no change in σ^2, however, this is unlikely given the established thermal dependence of σ^2. We observed similar behavior for $N_{Ge-Ge} \cdot \sigma^2_{Ge-Ge}$ (Fig. S8), however, due to the higher signal of the Ge−Te path in $|\chi(R)|$, the parameters for the Ge−Ge path have a higher level of statistical uncertainty.

Linear regressions to $N_{Ge-Te} \cdot \sigma^2_{Ge-Te}$ as a function of temperature highlight composition-dependent slopes (Fig. 5). The slopes for GST and GST-6% are steeper than those for GST-2% and GST-4%, reflecting the more pronounced temperature-dependent dampening of $|\chi(R)|$ in the GST and GST-6% spectra (Fig. 2). Values for the slopes and R^2 values for the linear regressions are reported in Table S2.

Since N and σ^2 are conflated, the observed difference in slopes can result from either a higher rate of increase in σ^2 or constant increase in σ^2 paired with a linear decrease in N. A higher rate of increase in σ^2 suggests that σ^2_{Ge-Te} in GST and GST-6% is more susceptible to temperature, which would result from the Ge−Te bonds being less rigid (i.e., weaker) in GST and GST-6% than in GST-2% and GST-4%.[29,35,41] This could explain why carbon-doping increases the stability of the amorphous state at low concentrations, specifically: the presence of C strengthens Ge−Te bonds and stabilizes the structure. We speculate that this interpretation of the observed parameter trends is more likely than the alternative, i.e., that Ge coordination decreases with increasing temperature. Simply, a linear increase in σ^2 is a commonly observed and well-modeled phenomenon,[35–38,40] while a gradual change in atomic coordination, unaccompanied by any indication of a phase change, is not.

Overall, this behavior indicates an effect of C on the strength of the Ge−Te bond, the coordination of Ge by Te, or both when C is in small concentrations (GST-2% and GST-4%). This effect is suppressed for a larger concentration of C (GST-6%), perhaps indicating that a secondary mode of C incorporation is active at higher C concentrations, which stabilizes the amorphous phase through a different mechanism. Literature has suggested the existence of multiple distinct modes of C incorporation into GST, consisting of the formation of Ge−C bonds at low levels,[16,23] then Sb−C bonds[16] and/or the formation of C=C chains[15,23,24] at higher doping concentrations.

Further Discussion

The changes in crystallization onset temperatures reported here are inconsistent with T_C measured on identically-prepared films[14] and other work on GST-C.[15,16,23,24] In literature, crystallization is typically ascribed to the emergence of crystalline diffraction peaks and/or drastic changes in film reflectivity or sheet resistance, which always coincide at the same temperature.[14–16,23,24] In contrast, crystallization onset temperature is defined here as the first temperature at which the features of the XANES spectra change. This is associated with a change in the local (0 Å to 12 Å) Ge environment in corresponding Fourier transformed

EXAFS spectra (Fig. S5). In particular, features in $\chi(R)$ emerge beyond the first coordination shell, which indicate an increase in crystallinity. However, EXAFS is only sensitive to half-path lengths (and thus, atomic correlations) as long as ≈ 12 Å. The inconsistency between XAS and XRD-derived crystallization temperatures could be due to an intermediate state of crystallinity, such as the formation of small (sub-nanometer) crystallization seeds which are ordered, but do not have sufficient periodicity for diffraction.[17,21,24,32,42–44] Alternatively, this behavior may be attributed to an intermediate separating phase, such as pure Ge, which has been detected briefly before GST crystallization.[20,45] Overall, it is difficult to compare GST crystallization mechanisms across literature, since reported crystallization behavior depends on temperature and time spent at that temperature, film thickness, film substrate, and capping layer (often TiN).[20,21,31,44,45]

In the context of the literature, our findings imply a more complex transition from short- to long-range order upon crystallization for GST and GST-C. A decoupling of the short-, medium-, and long-range order of phase change materials has been explored in computational studies[17,42,43] and may be key to reconciling the many conflicting reports regarding the structure and performance of GST and GST-C. Certainly, further work consisting of a ensemble of complementary characterization techniques such as *in situ* XAS, pair distribution function (PDF) analysis, XRD, Raman spectroscopy, and transmission electron microscopy (TEM) could fully explore the structure of GST across length scales, and each structural feature's effect on bulk properties.

For example, in addition to element-specific local structure information provided by XAS, Raman spectroscopy can provide sensitivity to carbon (particularly C$-$C bonds and their geometry)[15,46] and the geometry of Ge$-$Te and Sb$-$Te polyhedral units.[46] At the mid-range, PDF analysis can provide useful structural information, such as the formation of crystalline seeds, however we note the difficulties of this method on thin film samples.[47,48] As for long-range structure, in addition to diffraction studies, TEM can reveal spatially resolved information, such as the size, morphology, and distribution of crystalline and amorphous domains.[15,20,23,24,45,49]

Conclusions

In previous reports, X-ray diffraction (XRD) and resistivity measurements have indicated a pronounced change of the crystallization temperature for GST with the addition of C.[14] Using XAS, we find a modest change in crystallization onset temperature, which we define as the first temperature at which the local environment of Ge begins to display an increase in crystallinity. Specifically, we detect a $\leq 10\,^{\circ}\mathrm{C}$ increase in crystallization onset temperature for the 2% and 4% C-doped samples, and an increase of no more than $20\,^{\circ}\mathrm{C}$ for GST-6%. These inconsistencies between macroscopic response (average structure and resistivity) and our local structure data require a reevaluation of our understanding of GST's hierarchical structure and its evolution during amorphous-to-crystalline phase transformations.

We find that C content affects the nature of local structure evolution preceding crystallization. Unexpectedly, the effects of C on the evolution of the local structure with temperature do not follow a simple trend. This is opposed to the simple trend between C concentration and phase stability; previous work reports a steady, monotonic increase in crystallization temperature (and thus, amorphous phase stability) as a function of C content up to ≈ 6 at% C, based on XRD and electronic properties.[14] However, as evident in Fig. 5, the Ge environment changes most dramatically with temperature for GST and GST-6%, while very little change is observed for GST-2% and GST-4%. We pose some explanations for the observed spectra changes, especially that C affects either the strength or the coordination of the Ge$-$Te bond, although further work is needed to more precisely determine how it does so. Further, the nonlinear trend between this behavior and C content may indicate two modes of C incorporation in GST that occur at low and high C concentrations. Indeed, other work has indicated the existence of two distinct models of C incorporation, e.g., distributed at low concentrations and clustered at higher concentrations.[15,16,23]

Finally, we report an approach to investigate the effects of light dopants on local structure of amorphous materials. While directly probing structural information (e.g., bond coordination) of light dopants remains elusive, we show how one may investigate the indirect effect of the dopant on heavier and/or more concentrated species by modulating the doping concentration and observing structural trends. Furthermore, when using XAS over a temperature series, correlated parameters, such as N and σ^2, can be constrained and how they change as a function of temperature can be modeled with greater certainty. We hope this methodology can inspire similar studies of doped amorphous chalcogenides for memory applications and beyond.

Experimental

Synthesis

Chalcogenide thin films were deposited onto fused silica substrates using direct current magnetron sputter methods. Deposition involved a Unifilm Co. PVD-300 system and sputter targets procured from Process Materials, Inc. This turbomolecular-pumped system was evacuated to a base pressure of $\leq 5 \times 10^{-7}$ Torr ($\leq 7 \times 10^{-5}$ Pa) prior to each deposition in order to establish a pristine environment for film growth. The vessel was then backfilled with ultra-high purity Ar (99.995%) and maintained at 10 mTorr for plasma-based sputter deposition. This system operates using a sputter-down configuration with substrates moved and rotated underneath targets for uniform deposition. Deposition temperature was estimated to be 60 °C.

Films were sputtered using stoichiometric targets meaning all species deposited as a film were originally present in a single sputter target. New targets were generally sputter conditioned for at least 1 hour prior to first film depositions. In addition, each pre-conditioned target was sputtered for ≈ 5 minutes to remove adventitious carbon or oxide prior to the start of each deposition. Film compositions were determined by Wavelength Dispersive Spectroscopy to be $Ge_2Sb_2Te_5$ or $(Ge_2Sb_2Te_5)_{1-x}C_x$ ($x = 0$, 0.02, 0.04, 0.06, and 0.12) within ± 0.5 at% (x within ± 0.005).[14] The electron microprobe used for characterization is a JEOL JXA-8530F field emission microanalyzer. A Charles Taylor multi-element standard 202 was employed for elemental quantification. Reported compositions are generally 50-point averages.

XAFS Data Collection

XAS data at the Ge K-edge (11103 eV) were collected at the Beamline for Materials Measurement (6-BM) at the National Synchrotron Lightsource-II at Brookhaven National Laboratory. Measurements were made from 200 eV below the edge to 650 eV past the edge in fluorescence mode. Linkam cells were used for *in situ* data collection during heating in air. For GST, GST-4%, and GST-6%, spectra were collected at 10 °C increments from 30 °C to 300 °C. For GST-2%, data were collected at 10 °C increments from 30 °C to 230 °C. After a 1 min dwell period at the set temperature, two consecutive scans were taken for improved statistics. The average standard deviation of data points between the two merged datasets (normalized) was ≈ 0.0015. For GST-12%, measurements were taken in 10 °C increments from 110 °C to 300 °C, with one scan taken at each temperature.

XAFS Data Reduction

To ensure accuracy and consistency, data reduction was performed identically on all datasets using ATHENA[50] and LARCH.[51] XAS data reduction comprised merging scans (when applicable), deglitching (removal of artifacts), edge normalization, and background subtraction. Edge energies were chosen by selecting the energy at the inflection point of the edge, i.e., the first peak in the first derivative of the spectrum. From reduced XAS data, EXAFS spectra were produced by a Fourier Transform with a k window of $2\,\text{Å}^{-1}$ to $11\,\text{Å}^{-1}$ applying a Hanning window. The uncertainty related to the value of $\chi(R)$ was determined to be $\pm 0.02\,\text{Å}^{-3}$ for all spectra, following the procedure developed by M. Newville *et al.*[52]

EXAFS Fitting

EXAFS fitting was performed using LARCH,[51] which employs a least-squares refinement approach. Only amorphous spectra were considered for EXAFS fitting. Fits were performed with a k-weighting of 2 on the EXAFS spectra in real space within an R-range of 1.5 Å to 3.5 Å. Certain measurements were omitted from analysis due to inconsistencies in acquired data, such as high noise and truncated energy. Additional details of excluded data are provided in the SI.

All reported fitting models each contain two paths: the Ge−Te first shell single scattering path and the Ge−Ge first shell single scattering path. The scattering amplitude and phase of the Ge−Ge path was calculated using a cluster derived from diamond-structured pure Ge, whose bond length (2.45 Å) and coordination (four) forms a local electronic environment similar to that of GST. Ge−Te paths were generated the same way, except the Ge atoms surrounding the central Ge were replaced with Te atoms. Both paths were calculated using FEFF[53] as a part of the XAS VIEWER interface employing LARCH.[51]

The Ge−Sb first shell single scattering path was not included in fitting models. While the atomic number of Sb ($Z = 51$) is similar enough to that of Te ($Z = 52$) that the scattering contributions of the species are impossible to distinguish,[3,15] previous studies have not detected the existence of Ge−Sb bonds using Sb K-edge XAS.[3,4,54]

The signal contribution of the Ge−C first shell single scattering path is small but qualitatively visible near 1.4 Å in doped samples (Fig. S4). Some individual fitting experiments were able to confirm the presence of Ge−C coordinations around 1.85 Å. However, this path could not be reliably fit, so the Ge−C path was omitted from reported models. Instead, the fitting window minimum was increased to 1.5 Å, omitting the signal contributions of the Ge−C path.

For ‘unconstrained’ fits, the path parameters were free to refine within broad, but physically meaningful, bounds. N was constrained to always be positive, and never exceed a sum of 6 for all paths. σ^2 was constrained within the typical bounds of this parameter, between

$0.002\,\text{Å}^2$ and $0.02\,\text{Å}^2$.[33] r was constrained to never deviate by more than $0.1\,\text{Å}$ from its original value in the starting model. Incorporating parameters for the third cumulant did not meaningfully improve any fits and was thus avoided to reduce parameter correlations.[33,34]

Author Contributions

JDL: Conceptualization, data curation, formal analysis, investigation, methodology, validation, visualization, writing – original draft, writing – review & editing. DNA: Conceptualization, investigation. CG: Data curation, formal analysis, validation, visualization. BR: Investigation, validation, software. DA: Conceptualization, funding acquisition, project administration, resources, writing – original draft. MMB: Conceptualization, funding acquisition, methodology, project administration, resources, supervision, visualization, writing – original draft, writing – review & editing.

Acknowledgement

The authors thank Professor Thomas Beechem, Professor Alejandro Strachan, and Robert Appleton for helpful discussions about the structure of phase change materials. JDL also thanks Grant Bunker and Matt Newville for guidance on the theory and application of X-ray absorption spectroscopy.

This research utilized beamline 6-BM of the National Synchrotron Light Source II, a U.S. Department of Energy (DOE) Office of Science User Facility operated for the DOE Office of Science by Brookhaven National Laboratory under Contract No. DE-SC0012704.

This work was supported by the Sandia National Laboratory Directed Research and Development (LDRD) program. Sandia National Laboratories is a multi-mission laboratory managed and operated by National Technology and Engineering Solutions of Sandia, LLC. (NTESS), a wholly owned subsidiary of Honeywell International, Inc., for the U.S. Department of Energy's National Nuclear Security Administration (DOE/NNSA) under Contract

No. DE-NA0003525. This written work is authored by an employee of NTESS. The employee, not NTESS, owns the right, title, and interest in and to the written work and is responsible for its contents. This work describes objective technical results and analysis. Any subjective views or opinions that might be expressed in the paper do not necessarily represent the views of the U.S. Department of Energy or the U.S. Government. The publisher acknowledges that the U.S. Government retains a non-exclusive, paid-up, irrevocable, world-wide license to publish or reproduce the published form of this written work or allow others to do so, for U.S. Government purposes. The DOE will provide public access to results of federally sponsored research in accordance with the DOE Public Access Plan.

References

(1) Guo, P.; Sarangan, A. M.; Agha, I. A Review of Germanium-Antimony-Telluride Phase Change Materials for Non-Volatile Memories and Optical Modulators. *Appl. Sci.* **2019**, *9*.

(2) Wang, Q.; Niu, G.; Wang, R.; Luo, R.; Ye, Z.-G.; Bi, J.; Li, X.; Song, Z.; Ren, W.; Song, S. Reliable $Ge_2Sb_2Te_5$ based phase-change electronic synapses using carbon doping and programmed pulses. *J. Materiomics* **2022**, *8*, 382–391.

(3) Paesler, M.; Baker, D.; Lucovsky, G.; Edwards, A.; Taylor, P. EXAFS study of local order in the amorphous chalcogenide semiconductor $Ge_2Sb_2Te_5$. *J. Phys. Chem. Solids* **2007**, *68*, 873–877.

(4) Kolobov, A. V.; Fons, P.; Frenkel, A. I.; Ankudinov, A. L.; Tominaga, J.; Uruga, T. Understanding the phase-change mechanism of rewritable optical media. *Nat. Mater.* **2004**, *3*, 703–708.

(5) Ding, F.; Peng, B.; Li, X.; Zhang, L.; Wang, R.; Song, Z.; Huang, R. A review of compact modeling for phase change memory. *J. Semicond.* **2022**, *43*, 023101, Publisher: Chinese Institute of Electronics.

(6) Shafiee, A.; Pasricha, S.; Nikdast, M. A Survey on Optical Phase-Change Memory: The Promise and Challenges. *IEEE Access* **2023**, *11*, 11781–11803, Conference Name: IEEE Access.

(7) Gallo, M. L.; Sebastian, A. An overview of phase-change memory device physics. *J. Phys. D Appl. Phys.* **2020**, *53*, 213002, Publisher: IOP Publishing.

(8) Wuttig, M.; Raoux, S. The Science and Technology of Phase Change Materials. *Zeitschrift für anorganische und allgemeine Chemie* **2012**, *638*, 2455–2465.

(9) Ha, Y.; Yi, J.; Horii, H.; Park, J.; Joo, S.; Park, S.; Chung, U.-I.; Moon, J. An edge contact type cell for phase change RAM featuring very low power consumption. 2003 Symposium on VLSI Technology. Digest of Technical Papers (IEEE Cat. No. 03CH37407). 2003; pp 175–176.

(10) Washington, J. S. P. The local structure and kinetics of germanium-antimony-tellurium phase change materials for use in solid state applications. Ph.D. thesis, 2010; Copyright - Database copyright ProQuest LLC; ProQuest does not claim copyright in the individual underlying works; Last updated - 2023-03-03.

(11) Chung, H.; Jeong, B. H.; Min, B.; Choi, Y.; Cho, B.-H.; Shin, J.; Kim, J.; Sunwoo, J.; Park, J.-m.; Wang, Q., et al. A 58nm 1.8 V 1 Gb PRAM with 6.4 MB/s program BW. 2011 IEEE International Solid-State Circuits Conference. 2011; pp 500–502.

(12) Bez, R. Chalcogenide PCM: a memory technology for next decade. 2009 IEEE International Electron Devices Meeting (IEDM). 2009; pp 1–4.

(13) Zhou, W.; Wu, L.; Zhou, X.; Rao, F.; Song, Z.; Yao, D.; Yin, W.; Song, S.; Liu, B.; Qian, B.; Feng, S. High thermal stability and low density variation of carbon-doped $Ge_2Sb_2Te_5$ for phase-change memory application. *Appl. Phys. Lett.* **2014**, *105*, 243113.

(14) Scott, E. A.; Ziade, E.; Saltonstall, C. B.; McDonald, A. E.; Rodriguez, M. A.; Hopkins, P. E.; Beechem, T. E.; Adams, D. P. Thermal conductivity of $(Ge_2Sb_2Te_5)_{1\text{-}x}C_x$ phase change films. *J. Appl. Phys.* **2020**, *128*, 155106.

(15) Li, T.; Wu, L.; Ji, X.; Zheng, Y.; Liu, G.; Song, Z.; Shi, J.; Zhu, M.; Song, S.; Feng, S. Carbon doping induced Ge local structure change in as-deposited $Ge_2Sb_2Te_5$ film by EXAFS and Raman spectrum. *AIP Adv.* **2018**, *8*.

(16) Han, J. H.; Jeong, H.; Park, H.; Kwon, H.; Kim, D.; Lim, D.; Baik, S. J.; Kwon, Y.-K.; Cho, M.-H. Enhanced reliability of phase-change memory via modulation of local structure and chemical bonding by incorporating carbon in $Ge_2Sb_2Te_5$. *RSC Adv.* **2021**, *11*, 22479–22488.

(17) Hirata, A.; Ichitsubo, T.; Guan, P.; Fujita, T.; Chen, M. Distortion of local atomic structures in amorphous Ge-Sb-Te phase change materials. *Phys. Rev. Lett.* **2018**, *120*, 205502.

(18) Seo, H. S. H.; Jeong, T.-H. J. T.-H.; Park, J.-W. P. J.-W.; Yeon, C. Y. C.; Kim, S.-J. K. S.-J.; Kim, S.-Y. K. S.-Y. Investigation of Crystallization Behavior of Sputter-Deposited Nitrogen-Doped Amorphous $Ge_2Sb_2Te_5$ Thin Films. *Jpn. J. Appl. Phys.* **2000**, *39*, 745.

(19) Lai, Y.; Qiao, B.; Feng, J.; Ling, Y.; Lai, L.; Lin, Y.; Tang, T.; Cai, B.; Chen, B. Nitrogen-doped $Ge_2Sb_2Te_5$ films for nonvolatile memory. *J. Electron. Mater.* **2005**, *34*, 176–181.

(20) Agati, M.; Renaud, F.; Benoit, D.; Claverie, A. In-situ transmission electron microscopy studies of the crystallization of N-doped Ge-rich GeSbTe materials. *MRS Comm.* **2018**, *8*, 1145–1152.

(21) Thomas, O.; Mocuta, C.; Putero, M.; Richard, M.-I.; Boivin, P.; Arnaud, F. Crystallization behavior of N-doped Ge-rich GST thin films and nanostructures: An in-situ synchrotron X-ray diffraction study. *Microelectron. Eng.* **2021**, *244*, 111573.

(22) Park, S. J.; Jang, M. H.; Park, S. J.; Ahn, M.; Park, D. B.; Ko, D.-H.; Cho, M.-H. Effect of amorphization on the structural stability and reversibility of $Ge_2Sb_2Te_5$ and oxygen incorporated $Ge_2Sb_2Te_5$ films. *J. Mater. Chem.* **2012**, *22*, 16527–16533.

(23) Li, T.; Shen, J.; Wu, L.; Song, Z.; Lv, S.; Cai, D.; Zhang, S.; Guo, T.; Song, S.; Zhu, M. Atomic-Scale observation of carbon distribution in high-performance carbon-doped $Ge_2Sb_2Te_5$ and Its influence on crystallization behavior. *J. Phys. Chem. C* **2019**, *123*, 13377–13384.

(24) Zhou, X.; Xia, M.; Rao, F.; Wu, L.; Li, X.; Song, Z.; Feng, S.; Sun, H. Understanding Phase-Change Behaviors of Carbon-Doped $Ge_2Sb_2Te_5$ for Phase-Change Memory Application. *ACS Appl. Mater. Interfaces* **2014**, *6*, 14207–14214, PMID: 25090618.

(25) Song, Z. T.; Cai, D. L.; Li, X.; Wang, L.; Chen, Y. F.; Chen, H. P.; Wang, Q.; Zhan, Y. P.; Ji, M. H. High Endurance Phase Change Memory Chip Implemented based on Carbon-doped $Ge_2Sb_2Te_5$ in 40 nm Node for Embedded Application. 2018 IEEE International Electron Devices Meeting (IEDM). 2018; pp 27.5.1–27.5.4.

(26) Choi, Y. G.; Shin, S. Y.; Golovchak, R.; ki Cheong, B.; Jain, H. Comparative study of atomic arrangements in equiatomic GeSe and GeTe films before and after crystallization. *J. Alloys Compd.* **2016**, *686*, 273–280.

(27) Betti Beneventi, G. et al. Carbon-doped GeTe: A promising material for Phase-Change

Memories. *Solid-State Electron.* **2011**, *65-66*, 197–204, Selected Papers from the ESSDERC 2010 Conference.

(28) Ghezzi, G. E.; Raty, J. Y.; Maitrejean, S.; Roule, A.; Elkaim, E.; Hippert, F. Effect of carbon doping on the structure of amorphous GeTe phase change material. *Appl. Phys. Lett.* **2011**, *99*, 151906.

(29) Shin, S. Y.; Kim, H.; Golovchak, R.; ki Cheong, B.; Jain, H.; Choi, Y. G. Ovonic threshold switching induced local atomic displacements in amorphous $Ge_{60}Se_{40}$ film probed via in situ EXAFS under DC electric field. *J. Non-Cryst. Solids* **2021**, *568*, 120955.

(30) Michel, A.-K. U.; Sousa, M.; Yarema, M.; Yarema, O.; Ovuka, V.; Lassaline, N.; Wood, V.; Norris, D. J. Optical Properties of Amorphous and Crystalline GeTe Nanoparticle Thin Films: A Phase-Change Material for Tunable Photonics. *ACS Applied Nano Materials* **2020**, *3*, 4314–4320, Publisher: American Chemical Society.

(31) Cheng, H.-Y.; Raoux, S.; Chen, Y.-C. The impact of film thickness and melt-quenched phase on the phase transition characteristics of $Ge_2Sb_2Te_5$. *J. Appl. Phys.* **2010**, *107*, 074308.

(32) Allahyarov, E.; Sandomirski, K.; Egelhaaf, S. U.; Löwen, H. Crystallization seeds favour crystallization only during initial growth. *Nat. Commun.* **2015**, *6*, 7110, Publisher: Nature Publishing Group.

(33) Calvin, S. *XAFS For Everyone*; CRC Press: Boca Raton, 2013.

(34) Ravel, B.; Kelly, S. D. The Difficult Chore of Measuring Coordination by EXAFS. *AIP Conf. Proc.* **2007**, *882*, 150–152.

(35) Yang, C.; Paesler, M.; Sayers, D. Determination of bond strengths of arsenic and arsenic

chalcogen compounds using the temperature dependence of extended x-ray-absorption fine structure. *Phys. Rev. B* **1987**, *36*, 980.

(36) Abd el All, N.; Thiodjio Sendja, B.; Grisenti, R.; Rocca, F.; Diop, D.; Mathon, O.; Pascarelli, S.; Fornasini, P. Accuracy evaluation in temperature-dependent EXAFS measurements of CdTe. *J. Synchrotron Radiat.* **2013**, *20*, 603–613.

(37) Beni, G.; Platzman, P. Temperature and polarization dependence of extended x-ray absorption fine-structure spectra. *Phys. Rev. B* **1976**, *14*, 1514.

(38) Fornasini, P.; Grisenti, R. On EXAFS Debye-Waller factor and recent advances. *J. Synchrotron Radiat.* **2015**, *22*, 1242–1257.

(39) Fontana, M.; Lottici, P.; Razzetti, C.; Bianchi, D.; Antonioli, G.; Emiliani, U. Temperature dependence of EXAFS in amorphous arsenic. *Solid State Commun.* **1982**, *43*, 561–565.

(40) Lottici, P. P.; Antonioli, G.; Razzetti, C. Bond strengths in defect chalcopyrite $ZnGa_2Se_4$ by temperature dependence of EXAFS. *J. Phys. Chem. Solids* **1988**, *49*, 1057–1061.

(41) Maeda, Y.; Wakagi, M. Ge K-Edge Extended X-Ray Absorption Fine Structure Study of the Local Structure of Amorphous GeTe and the Crystallization. *Jpn. J. Appl. Phys.* **1991**, *30*, 101.

(42) Huang, B.; Robertson, J. Bonding origin of optical contrast in phase-change memory materials. *Phys. Rev. B* **2010**, *81*, 081204.

(43) Tavanti, F.; Dianat, B.; Catellani, A.; Calzolari, A. Hierarchical Short- and Medium-Range Order Structures in Amorphous Ge_xSe_{1-x} for Selectors Applications. *ACS Appl. Electron. Mater.* **2020**, *2*, 2961–2969.

(44) Fillot, F.; Sabbione, C. Nanoscale mechanics of thermally crystallized GST thin film by in situ x-ray diffraction. *J. Appl. Phys.* **2020**, *128*, 235107.

(45) Rahier, E.; Luong, M.-A.; Ran, S.; Ratel-Ramond, N.; Saha, S.; Mocuta, C.; Benoit, D.; Le-Friec, Y.; Claverie, A. Multistep Crystallization of Ge-Rich GST Unveiled by In Situ synchrotron X-ray diffraction and (scanning) transmission electron microscopy. *physica status solidi (RRL) – Rapid Research Letters* **2023**, *17*, 2200450.

(46) Němec, P.; Nazabal, V.; Moreac, A.; Gutwirth, J.; Beneš, L.; Frumar, M. Amorphous and crystallized Ge–Sb–Te thin films deposited by pulsed laser: Local structure using Raman scattering spectroscopy. *Mater. Chem. Phys.* **2012**, *136*, 935–941.

(47) Shamoto, S.; Yamada, N.; Matsunaga, T.; Proffen, T.; Richardson, J., J. W.; Chung, J.-H.; Egami, T. Large displacement of germanium atoms in crystalline $Ge_2Sb_2Te_5$. *Appl. Phys. Lett.* **2005**, *86*, 081904.

(48) Jensen, K. M. ; Blichfeld, A. B.; Bauers, S. R.; Wood, S. R.; Dooryhée, E.; Johnson, D. C.; Iversen, B. B.; Billinge, S. J. L. Demonstration of thin film pair distribution function analysis (tfPDF) for the study of local structure in amorphous and crystalline thin films. *IUCrJ* **2015**, *2*, 481–489.

(49) Rahier, E.; Ran, S.; Ratel Ramond, N.; Ma, S.; Calmels, L.; Saha, S.; Mocuta, C.; Benoit, D.; Le Friec, Y.; Luong, M. A.; Claverie, A. Crystallization of Ge-Rich GeSbTe Alloys: The Riddle Is Solved. *ACS Appl. Electron. Mater.* **2022**, *4*, 2682–2688.

(50) Ravel, B.; Newville, M. *ATHENA*, *ARTEMIS*, *HEPHAESTUS*: data analysis for X-ray absorption spectroscopy using *IFEFFIT*. *J. Synchrotron Radiat.* **2005**, *12*, 537–541.

(51) Newville, M. Larch: An Analysis Package For XAFS And Related Spectroscopies. *J. Phys. Conf. Ser.* **2013**, *430*.

(52) Newville, M.; Boyanov, B.; Sayers, D. Estimation of uncertainties in XAFS data. *J. Synchrotron Radiation* **1999**, *6*, 264–5.

(53) Rehr, J. J.; Kas, J. J.; Vila, F. D.; Prange, M. P.; Jorissen, K. Parameter-free calculations of X-ray spectra with FEFF9. *Phys. Chem. Chem. Phys.* **2010**, *12*, 5503–5513.

(54) Baker, D.; Paesler, M.; Lucovsky, G.; Agarwal, S.; Taylor, P. Application of bond constraint theory to the switchable optical memory material $Ge_2Sb_2Te_5$. *Phys. Rev. Lett.* **2006**, *96*, 255501.